



Selective photocatalytic reduction of nitroarenes into amines based on cobalt/copper ferrite and cobalt-doped copper ferrite nano-photocatalyst

Mai M. El-Masry¹, Mahmoud El-Shahat^{2,*} , Rania Ramadan³, and Reda M. Abdelhameed^{4,*}

¹Basic Science Department, Higher Engineering Institute, Thebes Academy, Cairo, Egypt

²Photochemistry Department, Chemical Industries Research Division, National Research Centre, 33 EL Buhouth St., Dokki 12622, Giza, Egypt

³Materials Science Laboratory (1), Physics Department, Faculty of Science, Cairo University, Giza, Egypt

⁴Applied Organic Chemistry Department, Chemical Industries Research Division, National Research Centre, 33 EL Buhouth St., Dokki 12622, Giza, Egypt

Received: 14 March 2021

Accepted: 10 June 2021

Published online:
22 June 2021

© The Author(s), under exclusive licence to Springer Science+Business Media, LLC, part of Springer Nature 2021

ABSTRACT

The reductions of nitro groups in nitroaromatic compounds to amino-aromatic have great opportunities in synthetic chemistry. Previously the process of nitroaromatic reduction used catalytic systems operated under hard conditions, leading to missing the pure and high yield of the final products. Here, a cobalt ferrite, copper ferrite, and cobalt-doped copper ferrite nanocatalyst were prepared using the citrate spontaneous combustion method. In addition to the properties of the prepared nanocatalyst, the present methodology describes the effective reduction of a variety of nitroaromatic compounds into corresponding anilines under visible light illumination. The cobalt-doped copper ferrite photocatalyst showed excellent activity up to 99% by converting nitroaniline into amino-aniline. The optimized catalytic conditions (room temperature, atmospheric pressure, and visible light irradiation) were applied in the reduction of a series of nitroarenes giving a high conversion rate (93–98%) and selectivity (95–99%). The photocatalytic system has the advantage due to the lack of filtration in the recycling experiments and the high stability of up to six cycles.

Address correspondence to E-mail: mahmoudelshahat@gmail.com; reda_nrc@yahoo.com

1 Introduction

Synthetic chemistry mainly depends on nitrogen-containing compounds because it has a wide range of applications in pharmaceutical industries, agrochemical synthesis, heterocyclic compounds, dyes, food additives, etc. [1]. Reducing nitrobenzene is a very important issue in a biological transformation due to it reduces the carcinogen and genotoxic substance nitrobenzene to the corresponding anilines [2]. In the manufacturing of anilines, benzene was treated with nitric acid and sulfuric acid under heating at a temperature of 50–60 °C followed by the catalytic hydrogenation of the compound nitrobenzene at 200–300 °C [3]. The disadvantage of this industrial process lies in consumes a huge amount of heat, which boosts the cost of the final product. However, there is no other commercial methodology available for the synthesis of aniline. Recently, the reduction of nitroaromatics takes place using photocatalysts. This process shows the perfect selectivity for the reduction of nitroanilines [4–6]. The previous work on the photocatalytic selective reduction of nitroaromatic compounds was focused on using TiO₂ [7], N-doped TiO₂ [8], and dye-sensitized TiO₂[9] under UV and visible light irradiation. Recently, the metal–organic framework [10–12] acts as a promising photocatalyst in the reduction of nitroaromatic because of its low bandgap and high stability. For example, CdS was added to UiO-66 giving high activity [13], moreover, Ag₂CrO₄ was decorated with NH₂-MIL-125 achieved high nitroaromatic reduction activity [14], recently, Pd was added to the film formed from MIL-125-NH₂ and Cellulose Acetate showing high catalytic performance [15]. As far as, the complexing agents have been used for synthesizing ferrites. For example, ethylenediamine [16] and sodium citrate [17] have been used to synthesize Co-based ferrites. Synthesis of Nanomagnets. like SmxCoy was prepared in Large-Scale using Flame-Reaction Method [18], the stabilization of SmCo₅ nanoparticles was done using an N-doped graphitic carbon layer[19].

Working with photocatalyst is a challenging item so searching for a new catalyst is so necessary. Recently, magnetic nanoparticles gain much attention due to their unique properties [20]. Spinel iron has been extensively studied in the nanostructure for its many interesting properties such as optical, chemical, electrical, and magnetic properties [21]. The use of

ferrite (metal oxides with iron as a major metallic component) as catalysts for both oxidation and reduction of organic pollutants, and the removal, degradation, or conversion of these pollutants is an inexpensive, easy, and widely applicable method. Ferrites are reusable magnetic separable heterogeneous catalysts that are practically applicable in wastewater treatment, cost-effective, and non-toxic. Pure phases of cobalt ferrite were obtained using the Pechini method and performed well in the degradation of diclofenac sodium by the Photo-Fenton process using germicidal irradiation of ultraviolet and H₂O₂ as the oxidant. [22]. Moreover, iron (II) was added to the copper ferrite to produce Cu^{II}_(x)Fe^{II}_(1-x)Fe^{III}₂O₄ nanoparticles. The photocatalytic applications of new materials were investigated for the decomposition of methylene blue (MB) and showed that iron (II) doped copper ferrite, due to its favorable bandgap energies and characteristic structures, exhibit strong photolysis potential of dyes [23]. In addition, adding a small percentage of aluminum to different metallic iron results in a significant change like ferrite to have photosynthetic activity. The photocatalytic activity of the Al-doped ferrites was found in the order, Zn > Co > Cu > Ni > Cd > Cr ferrites for dye decomposition [24]. A novel unconventional precipitation procedure followed by a simple and rapid microwave-assisted hydrothermal treatment was used to synthesize a novel nanomaterial cobalt ferrite with Fenton photoactivity. Co-ferrite nanoparticles were obtained at room temperature in the absence of surfactants and Fenton photosynthetic activity was evaluated by lignin hydrolysis [25]. GO-doped metal ferrites (GO-Fe₃O₄ and GO-CoFe₂O₄) were prepared and its photocatalytic potentials were investigated against acetamiprid's degradation [26]. Fe₃O₄-Cu nanocomposite catalyst is versatile towards carbonyl and nitro reduction under mild reaction conditions with very good yield and turnover number [27]. In this study, CoFe₂O₄, CuFe₂O₄, and Cu-CoFe₂O₄ nanoparticles were synthesized and characterized using different techniques. Besides investigation, the structure of the prepared compounds, the photocatalytic reduction of nitroaromatics compounds were investigated. The eco-friendly magnetic photocatalysts were synthesized and the possible organic nitro compounds photoreduction mechanisms were studied.

2 Experimental

2.1 Materials

Iron nitrate $\text{Fe}(\text{NO}_3)_3 \cdot 9\text{H}_2\text{O}$ (99%), cobalt nitrate $\text{Co}(\text{NO}_3)_2 \cdot 0.6\text{H}_2\text{O}$, copper nitrate and $\text{Cu}(\text{NO}_3)_2 \cdot 6\text{H}_2\text{O}$ (99%) were used as mineral precursors, 4-nitroaniline, citric acid anhydrous ($\text{C}_6\text{H}_8\text{O}_7$, 99.57%), and nitroaromatic compounds were purchased from Aldrich.

2.2 Nano-powder preparation

CoFe_2O_4 , CuFe_2O_4 , and $\text{Cu-CoFe}_2\text{O}_4$ nanoparticles were synthesized using the citrate spontaneous combustion method. CoFe_2O_4 was synthesized as follows: cobalt nitrate (2.91 g, 0.01 mol) and iron nitrate (4.04 g, 0.01 mol) were added to a 50 mL aqueous solution of (1.92 g, 0.01 mol) citric acid. The mixture was vigorously stirring for 6 h at room temperature. Then the pH value of the solution was adjusted to 7.0. The temperature was raised to 250° C to obtain a fine powder. The final powder was roasted for 4 h at 800° C at a rate of 4° C/min. CuFe_2O_4 was prepared as above except cobalt nitrate was replaced by copper nitrate (2.95 g, 0.01 mol). A $\text{Cu-CoFe}_2\text{O}_4$ nanoparticle was prepared as follows: cobalt nitrate (1.45 g, 0.005 mol), copper nitrate (1.47 g, 0.005 mol), and iron nitrate (4.04 g, 0.01 mol) were added to 50 mL aqueous solution of (1.92 g, 0.01 mol) citric acid. The above procedures were applied to obtain the final material.

2.3 Nano-powder characterization

Structural characterization of samples was performed by X-ray powder diffraction (XRD) using a $\text{CuK}\alpha$ -irradiated Proker D8 X-ray pre-diffractometer ($\lambda = 1.5418 \text{ \AA}$). High-Resolution Transmission Electron Microscope (HRTEM) JEM-ARM300F operating at 200 kV. X-ray Photoelectron Spectroscopy (XPS) spectra were obtained using a spectrometer (model Thermo Scientific K-Alpha) with a monochromatic X-ray source of $\text{AlK}\alpha$. The acquisition time is 10 min for all samples, several scans were 20, the spot size of 400 μm , lens mode was standard, analyzer mode (CAE: Pass Energy 50.0 eV) with an energy step size of 0.100 eV and number of energy steps 601. Infrared (IR) spectra were recorded for all samples by FTIR instrument (Perkin Elmer) in the range of

4000–400 cm^{-1} . The surface area determined by the N_2 absorption method was determined using a BET Multi-point (St 2 on NOVA touch 4LX [s / n: 17016062702]). Optical properties were analyzed with a UV–vis Spectrophotometer (JASCO Corp., V-570, Rev.100).

2.4 Photocatalytic activity measurement

Photocatalytic activities were evaluated under visible light. The irradiation source was a 500-W Philip lamp. In all the photocatalytic reduction experiments, 25 mg of the CoFe_2O_4 , CuFe_2O_4 , and $\text{Cu-CoFe}_2\text{O}_4$ nanoparticles were added to 100 mL of nitroaniline solution (20 mg L^{-1}). Before irradiation, suspensions containing nitroaniline and photocatalysts were magnetically stirred in the dark for 30 min. to ensure absorption/adsorption equilibrium was established. At a specified period, 5 ml aliquots were sampled and then magnetically separated to essentially remove all of the stimuli. The filtration was analyzed by recording the differences in the maximum absorption band with a Shimadzu UV-2550 UV–vis spectrophotometer.

3 Results and discussion

3.1 Characterization

3.1.1 XRD

XRD patterns of the CoFe_2O_4 , CuFe_2O_4 , and $\text{Cu-CoFe}_2\text{O}_4$ samples are shown in Fig. 1a–c. Remarked diffraction peaks at $2\theta = 30.61^\circ$, 35.46° , 38.48° , 43.06° , 53.62° , 57.01° are concerned to (2,2,0), (3,1,1), (2,2,2), (4,0,0), (4,2,2) and (5,1,1) planes of ferrite structure, the XRD results for all prepared samples correspond to the standard stage reported in the ICDD reference XRD card. Nanoparticle size was calculated using the X-ray line expansion method via the Scherer equation (Eq. 1)[28].

$$D = \frac{k\lambda}{\beta \cos \theta} \quad (1)$$

where D is the crystal size (nanometers), K is the particle form factor, is the target wavelength (nm), is the full width corrected by the maximum half, and is the position (angle) of the peak at the maximum. Both the instrument and the sample affect the full Bragg peak width at half-maximum (FWHM), and the

Fig. 1 XRD spectrum of (a): CuFe_2O_4 , (b): CoFe_2O_4 , (c): $\text{Cu-CoFe}_2\text{O}_4$

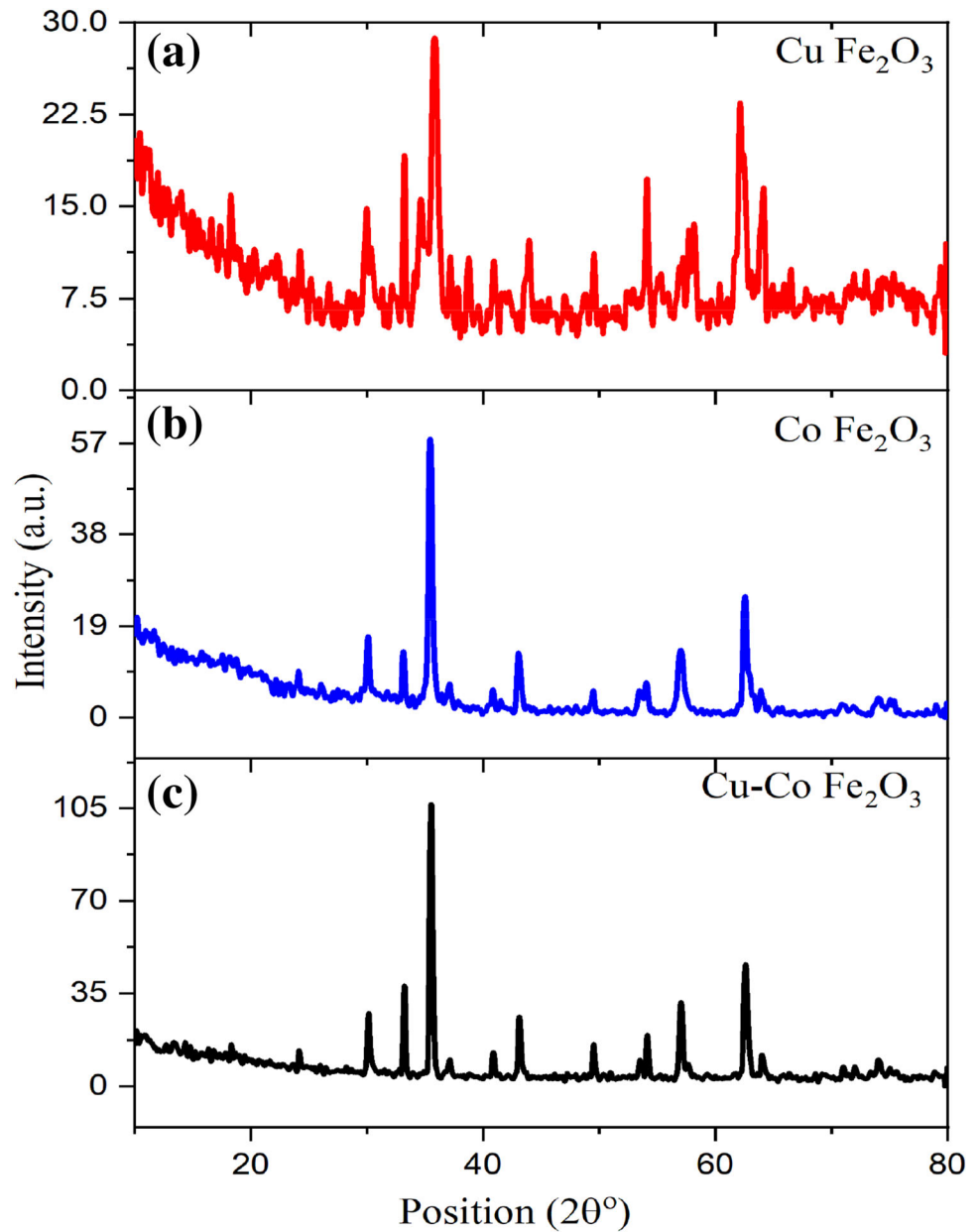


Table 1 The crystal systems, cell parameter, cell volume and the estimated particle sizes of CoFe_2O_4 , CuFe_2O_4 and $\text{Cu-CoFe}_2\text{O}_4$

Sample	Crystal system	a (Å)	b (Å)	c (Å)	Cell volume (Å ³)	Average crystal size (nm)	
						XRD	TEM
CoFe_2O_4	Cubic	8.4	8.4	8.4	592.7	19.8	31.04
CuFe_2O_4	Tetragonal	5.89	5.89	8.56	297.25	24.1	53.1
$\text{Cu-CoFe}_2\text{O}_4$	Cubic	8.39	8.39	8.39	590.74	22.2	43.7

expansion of the XRD peaks is a combination of both. The network constant (a), cell volume (V), extracted from the XRD spectra were calculated using the

following relationships (Cullity & Weymouth, 1957)[29] and tabulated in Table 1:

$$a = d_{hkl} \sqrt{(h^2 + k^2 + l^2)}, V = a^3 \tag{2}$$

3.1.2 HRTEM

HRTEM micrographs shown in Fig. 2a–c of CoFe_2O_4 , CuFe_2O_4 , and $\text{Cu-CoFe}_2\text{O}_4$ respectively showed a homogeneous distribution of polycrystalline nanometer particles. The nanoparticles consist of standardized cubic crystals with an average crystal size of 30.04 nm, 53.1, and 43.7 nm for CoFe_2O_4 , CuFe_2O_4 , and $\text{Cu-CoFe}_2\text{O}_4$, respectively (Table 1). These values are greater than those estimated from the XRD results. The present particles showed agglomeration as some of the particles formed large clusters.

3.1.3 FTIR

The FTIR spectra of the CoFe_2O_4 , CuFe_2O_4 , and $\text{Cu-CoFe}_2\text{O}_4$ nanoparticles were recorded in the range $4000\text{--}400\text{ cm}^{-1}$ and are illustrated in Fig. 3a–c, respectively. Figure 3a shows the FTIR spectra of CoFe_2O_4 nanoparticles. The band vibrations O–H interacting through H-bonds was observed at 3667.23 cm^{-1} , 2987 cm^{-1} , and 2901 cm^{-1} . The band at about 1406 cm^{-1} is due to the bending of water molecules [30]. The band at 1108 cm^{-1} may be due to residual FeOOH . The bands present at about 537.9 cm^{-1} , 471 cm^{-1} and 416.44 cm^{-1} are due to the band vibrations of the metal oxide in the octahedral group Co(II)-O^{2-} and Fe(III)-O^{2-} tetrahedral

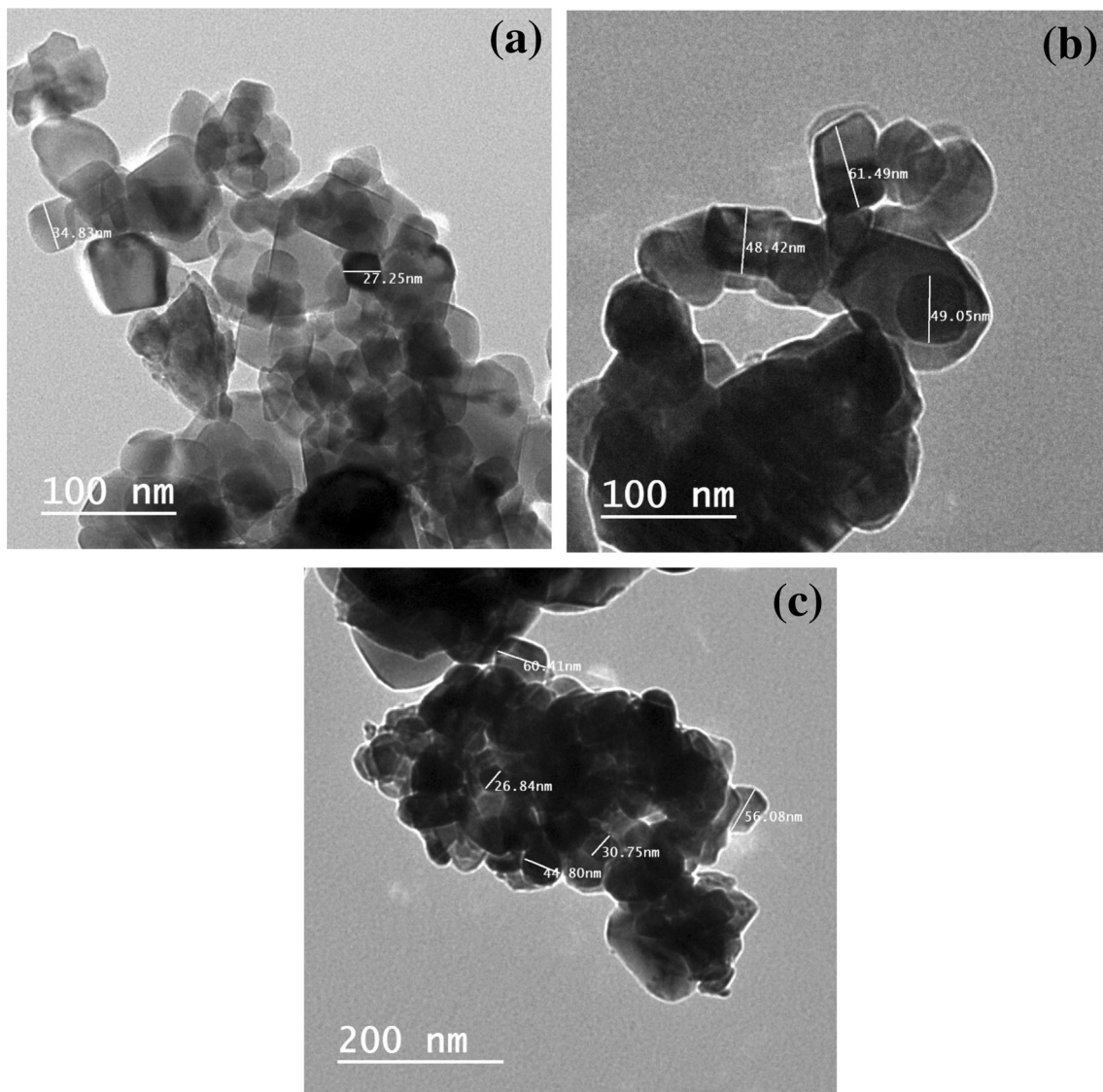
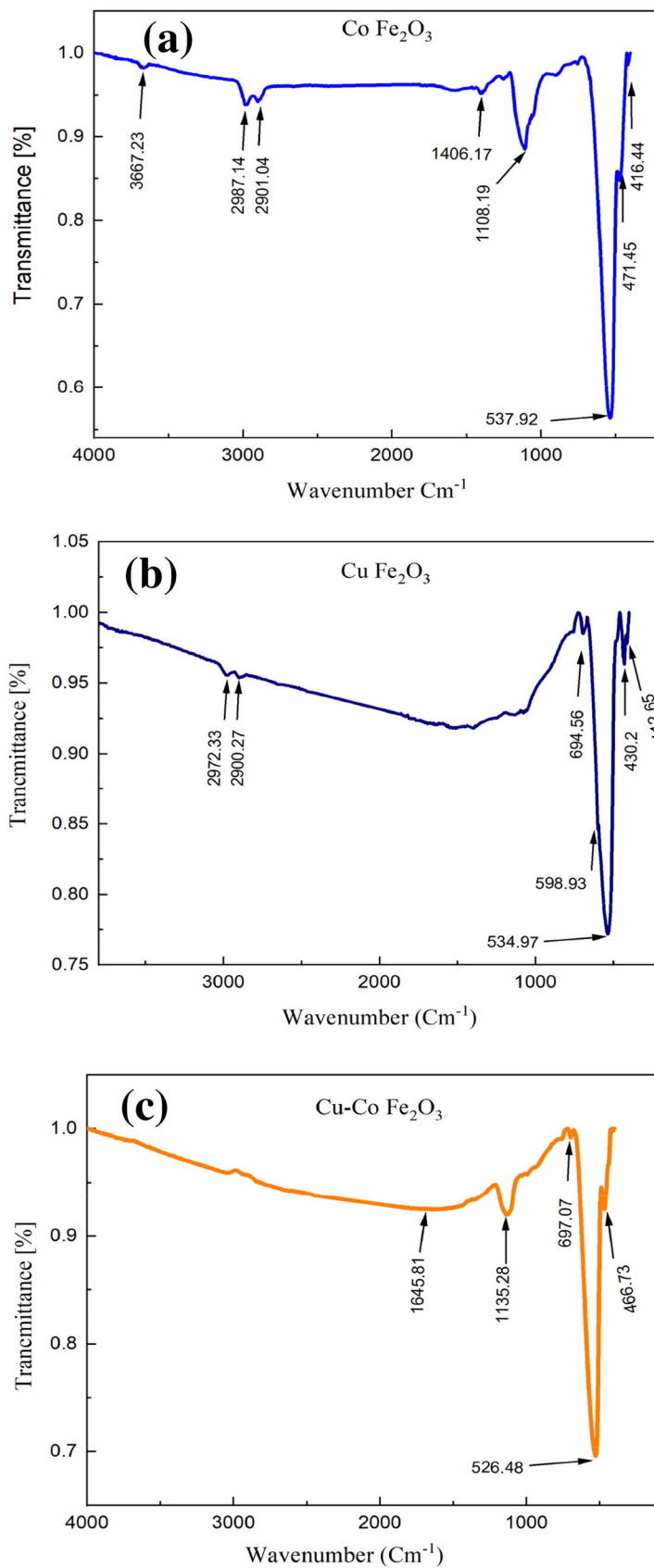


Fig. 2 HRTEM micrographs of (a): CoFe_2O_4 , (b): CuFe_2O_4 , (c): $\text{Co-CuFe}_2\text{O}_4$

Fig. 3 FTIR spectrum of (a): CoFe_2O_4 , (b): CuFe_2O_4 , (c): $\text{Co-CuFe}_2\text{O}_4$



group. The peaks in Fig. 3b showed the characteristic peaks of spinel-made ferrites located in the low wavelength range where the bands at 694.56 cm^{-1} , 598.93 cm^{-1} , 430.2 cm^{-1} , and 412.65 cm^{-1} , the MO (M) vibrations denoted by Cu or iron). The bands that appeared at 2972.33 cm^{-1} and 2900.27 cm^{-1} can be assigned to span the C-H = bond. From Fig. 3c, the bands in the region $400\text{--}600\text{ cm}^{-1}$ confirm the presence of copper iron. Moreover, the band observed around 526 cm^{-1} is assigned to the vibration of metal cations at the tetrahedral sites while the bands at 466 cm^{-1} are attributed to the vibration of the oxygen bonds [31, 32].

3.1.4 XPS

Figure 4 illustrates the XPS measurements carried out to investigate electronic state and cation distribution for the prepared CoFe_2O_4 , CuFe_2O_4 , and $\text{Cu-CoFe}_2\text{O}_4$ nanoparticles. The figure presents wide-scan spectra of these samples in the binding energy range 200 to 965 eV. The binding energies of the particles were calibrated by taking the C1s peak as reference (285 eV). The XPS spectra showed the existence of copper, cobalt, iron, and oxygen in the prepared samples. The XPS spectrum of Cu 2p of

copper ferrite and copper ferrite doped with cobalt samples, shown in Fig. 5a and b), exhibited the characteristic of Cu^+ with two main peaks of Cu $2p_{3/2}$ at 933 eV and Cu $2p_{1/2}$ 953 eV and two satellite peaks. It can be noted that the obtained spectra originated from the mixture of Cu^+ and Cu^{2+} ions [33]. The relative fraction (%) of ($\text{Cu}^+ / \text{Cu}^{2+}$) for each prepared sample is illustrated in Table 2. It can be observed that the relative fraction (%) of ($\text{Cu}^+ / \text{Cu}^{2+}$) for the CuFe_2O_4 sample was 48.5% and decreased to 41% by doping the sample with Cobalt indicating the strong interaction between copper and cobalt.

Figure 6a and b show the XPS spectrum of Co 2p of cobalt ferrite and copper ferrite doped with cobalt samples. The two deconvoluted peaks are associated with two spin-orbit doublets characteristics of Co $2p_{3/2}$ at 780 and 783.7 eV and peak at 796 eV corresponding to Co $2p_{1/2}$. The peaks are situated at $\sim 780\text{ eV}$, 783.7 eV which are associated with Co^{2+} ions at octahedral sites and tetrahedral sites of the spinel structure, respectively. In turn, the peak at 786.7 eV corresponds to a satellite peak associated with the high spin Co^{2+} in the octahedral position. The relative fractions of (Co^{2+} in octahedral / Co^{2+} in tetrahedral sites) % in both CoFe_2O_4 and $\text{Cu-CoFe}_2\text{O}_4$ samples are listed in Table 3. A decrease in the (Co^{2+}

Fig. 4 XPS spectrum of CuFe_2O_4 , CoFe_2O_4 , $\text{Co-CuFe}_2\text{O}_4$

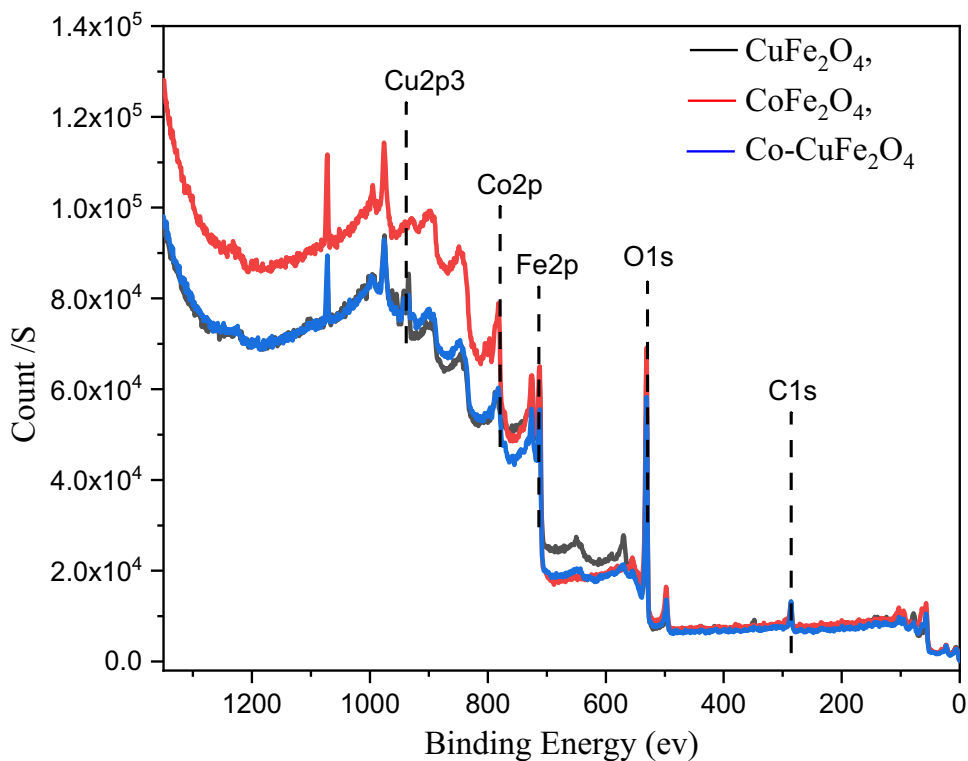
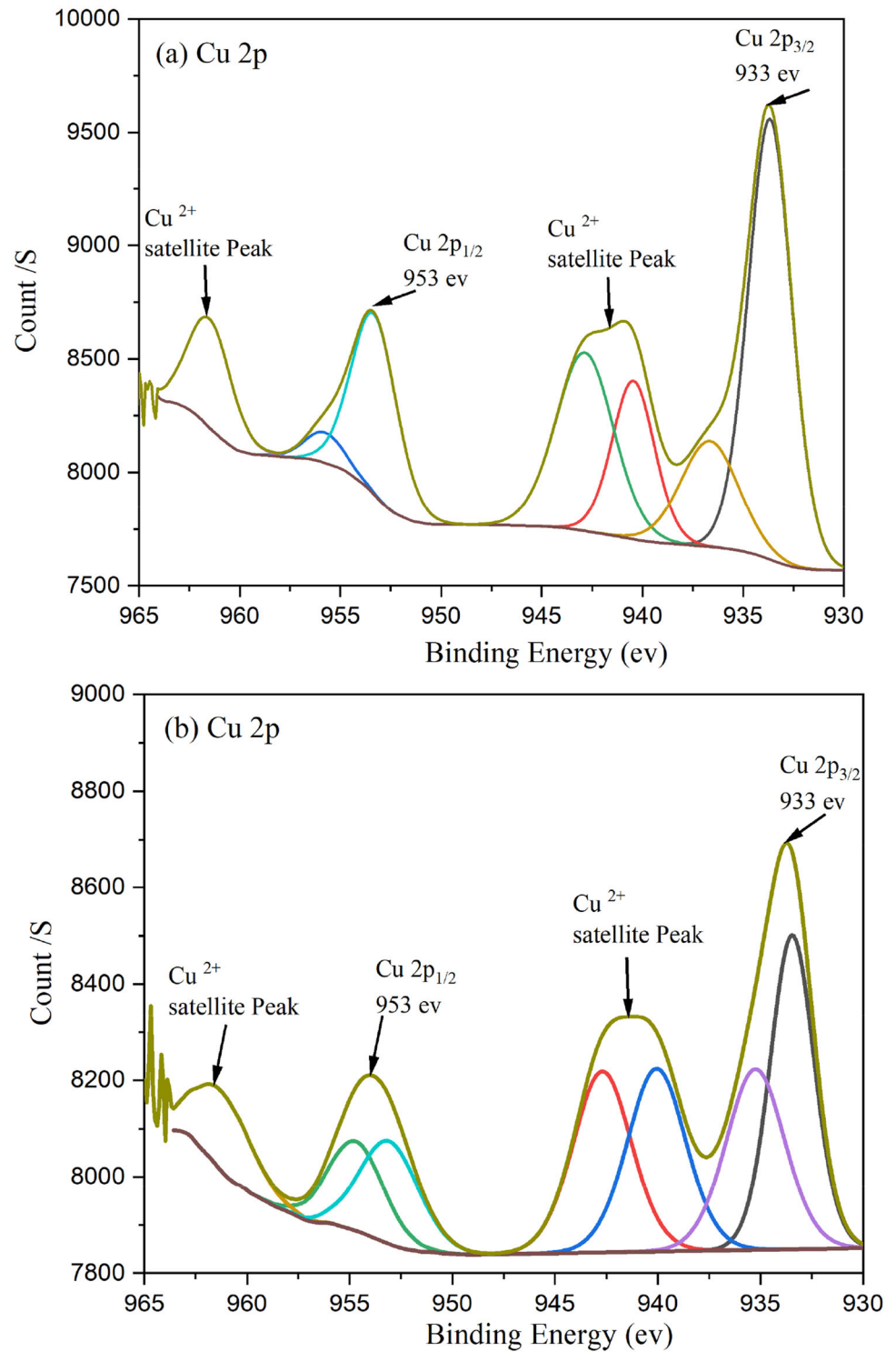


Fig. 5 XPS of Cu 2p spectrum in: (a) Copper ferrite and (b) in cobalt doped copper ferrite prepared samples



in octahedral / Co²⁺ in tetrahedral sites) % was recorded in the Cu-CoFe₂O₄ sample. This could be due to the site preference of copper ion for the octahedral site in cobalt ferrite. Substitution of metal ions in the octahedral site plays a crucial role in the

catalytic activity by acting as a medium for the transfer of electrons and hence higher catalytic activity.

Table 2 Binding energies of Cu 2p_{3/2}, Cu 2p_{1/2}, and the relative fraction (%) of oxidation state for CuFe₂O₄ and Cu-CoFe₂O₄ samples

Sample	Spin-orbit	Binding Energy (ev)	The relative fraction (%) of oxidation state
CuFe ₂ O ₄	Cu 2p _{3/2}	933	(Cu ⁺ /Cu ²⁺) %
	Cu 2p _{1/2}	953	(48.5) %
Cu-CoFe ₂ O ₄	Cu 2p _{3/2}	933	(Cu ⁺ /Cu ²⁺) %
	Cu 2p _{1/2}	953	(41) %

3.1.5 BET

The surface area test was performed with the N₂ adsorption method to obtain how the layers, size, and pores of CoFe₂O₄, CuFe₂O₄, and Cu-CoFe₂O₄ nanoparticles were formed. In Fig. S1(a, b, c) it can be seen that CoFe₂O₄ and CuFe₂O₄ follow the fourth type of isothermal curve based on the IUPAC classification system. This indicates a multilayer adsorption formation with a solid flat structure. The specific surface area of CoFe₂O₄ and CuFe₂O₄ were 27.9872 m²/g and 3.46399 m²/g, respectively [33].

3.1.6 Optical properties

Optical excitation is the production of an excited state of a quantum system by the absorption of a photon. In optical absorption, an electron is excited from the top of the valence band at the bottom of the conduction band across the energy bandgap [34]. The amount of light absorbed by any photocatalyst depends on the energy of the optical bandgap (the difference between the valence band and the conduction band). Across the bandgap, the transitions occur between the extended parity band states to the extended conduction band state that can be represented using the Tauc region (T region). In general, two types of transitions can occur at this basic edge: direct and indirect transitions. Both transformations involve the interaction of an electromagnetic wave with an electron in the valence band that is stimulated in the conduction band across the fundamental bandgap [35]. However, in the case of indirect transmission, a simultaneous reaction with network vibration also occurs. The bandgap (E_g) values can be calculated via Tauc's relationship using the following equation:

$$(\alpha h\nu)^n = A(h\nu - E_g) \quad (3)$$

where α is absorption coefficient, A is band edge parameter, n determines the nature of optical transition ($n = 2$ indicates direct transition and $n = 1/2$ indicates indirect transition) [10]. During this

transition process, if some perturbation is created due to the presence of local tail states that arose from defects in the microstructure, then the density of the electron states in the valence and tails of the conduction band in the energy gap. The electron state density tail extending into the energy bandgap is called the Urbach tail, which is related to the width of the local states available in the optical bandgap. The Urbach Eu energy has been well described under the Einstein model.

$$E_u = (E_u)_0 + (E_u)_1 \left[\frac{1}{e^{\left(\frac{\theta_E}{T} - 1\right)}} \right] \quad (4)$$

where $(E_u)_0$, $(E_u)_1$, are the constant values, θ_E is the Einstein temperature which corresponds to the average frequency of phonon excitations of noninteracting oscillations. These equations can be compressed into an empirical formula as follow:

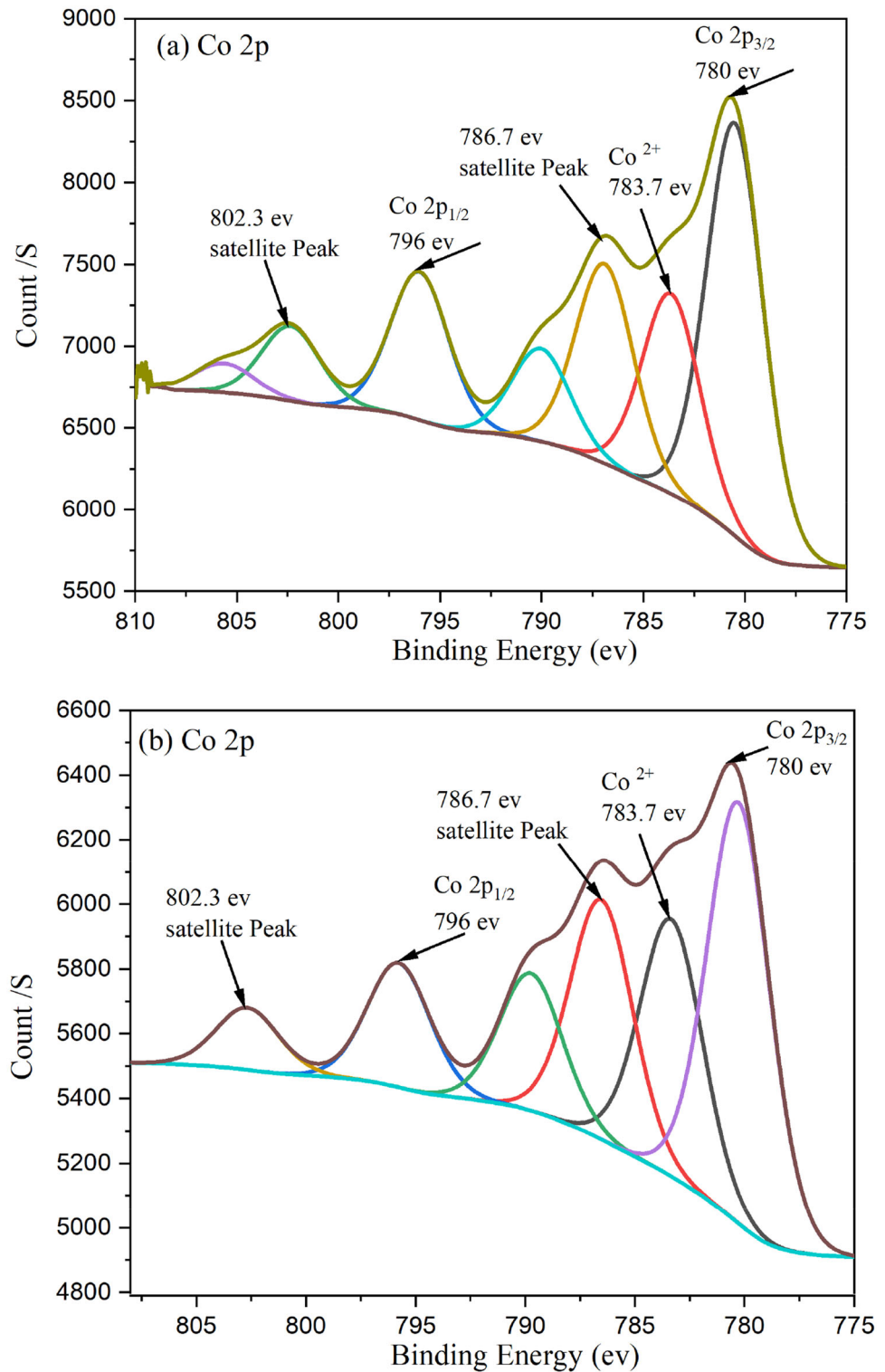
$$\alpha = \alpha_0 e^{\left(\frac{h\nu}{E_u}\right)} \quad (5)$$

The band tail energy or Urbach energy (E_u) can be obtained from the slope of the straight line of plotting $\ln(\alpha)$ against the incident photon energy ($h\nu$). E_u values were calculated from the reciprocal of the straight line slope.

$$E_u = \frac{1}{\text{Slope}} \quad (6)$$

The optical absorption spectra of the CoFe₂O₄, CuFe₂O₄, and Cu-CoFe₂O₄ nanocrystals were recorded using a visible UV-visible spectrophotometer. Figure 7 shows that the values of the absorption intensity for all examined samples was approximately 87–89% in the 450–1200 nm range covering the visible region, giving the prepared samples an important role in the photocatalytic reactions. Tauc model was used to estimate direct and indirect bandgap energies. Figure 8a–c show a plot of $(\alpha h\nu)^2$ versus the photon energy of CoFe₂O₄, CuFe₂O₄, and Cu-CoFe₂O₄ nanoparticles, respectively, photon energy (straight line interception on the x-axis) shows

Fig. 6 XPS of Co 2p spectrum in: (a) Cobalt ferrite and (b) in cobalt doped copper ferrite prepared samples



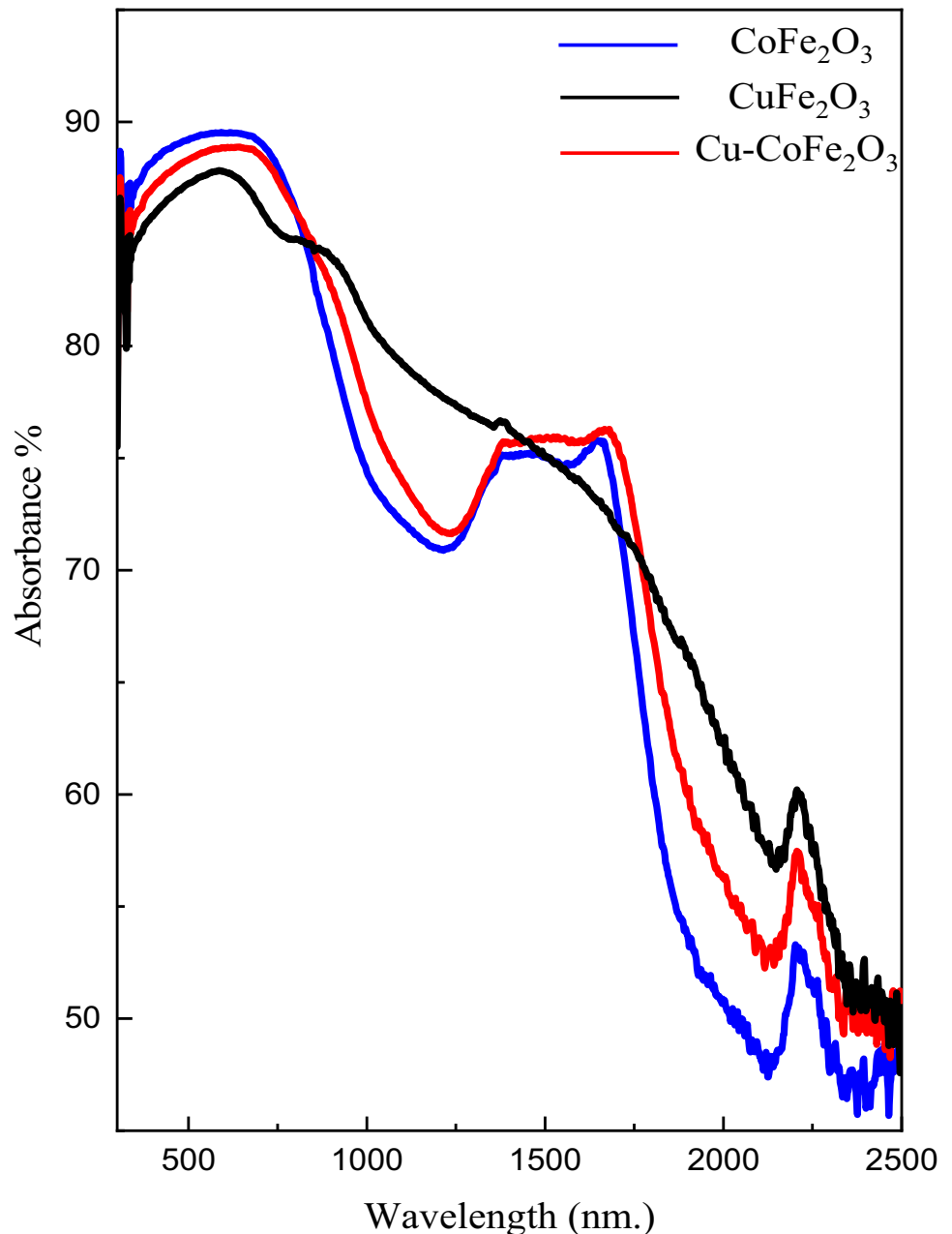
the direct bandgap of the CoFe_2O_4 nanoparticles and CuFe_2O_4 and $\text{Cu-CoFe}_2\text{O}_4$. The estimated direct bandgap values of Fig. 8a–c listed in Table 4, were found to be 1.11, 2.11, and 2.08, eV for CoFe_2O_4 , CuFe_2O_4 , and $\text{Cu-CoFe}_2\text{O}_4$, respectively. A significant change in the bandgap values of CoFe_2O_4 was

observed with doping with Cu^{2+} . A redshift was observed for Cu^{2+} doping in cobalt ferrite. This may be caused by defects and the formation of a sub-gap energy level in the nanoparticles. From these results, it can be concluded that Cu^{2+} doped CoFe_2O_4 NPs are visible active substances. Figure 8a–c, a plot of

Table 3 Binding energies of Co 2p_{3/2} Co 2p_{1/2} and the relative fraction (%) Co²⁺ in octahedral / Co²⁺ in tetrahedral sites for CoFe₂O₄, and Cu-CoFe₂O₄ samples

Sample	Spin-orbit	Binding Energy (ev)	(Co ²⁺ in octahedral / Co ²⁺ in tetrahedral sites) %
CoFe ₂ O ₄ ,	Co 2p _{3/2}	780, 783.7	67%
	Co 2p _{1/2}	796	
Cu-CoFe ₂ O ₄	Co 2p _{3/2}	780, 783.7	62%
	Co 2p _{1/2}	796	

Fig. 7 UV-Vis. Absorbance spectrum of (a): CoFe₂O₄, (b): CuFe₂O₄, (c): Co-CuFe₂O₄



$(\alpha h\nu)^{1/2}$ vs. photon energy reveals an indirect band-gap in CoFe₂O₄, CuFe₂O₄, and Cu-CoFe₂O₄, at 0.087, 0.31, and 0.32 eV, respectively. Comparing the indirect and direct gap values of the investigated samples

reveals that CoFe₂O₄, CuFe₂O₄, and Cu-CoFe₂O₄ display a fundamental indirect energy gap.

Figure S2(a,b, and c) shows the variation of the absorption coefficient (α) of CoFe₂O₄, CuFe₂O₄, and Cu-CoFe₂O₄ as a function of wavelength (300–2500)

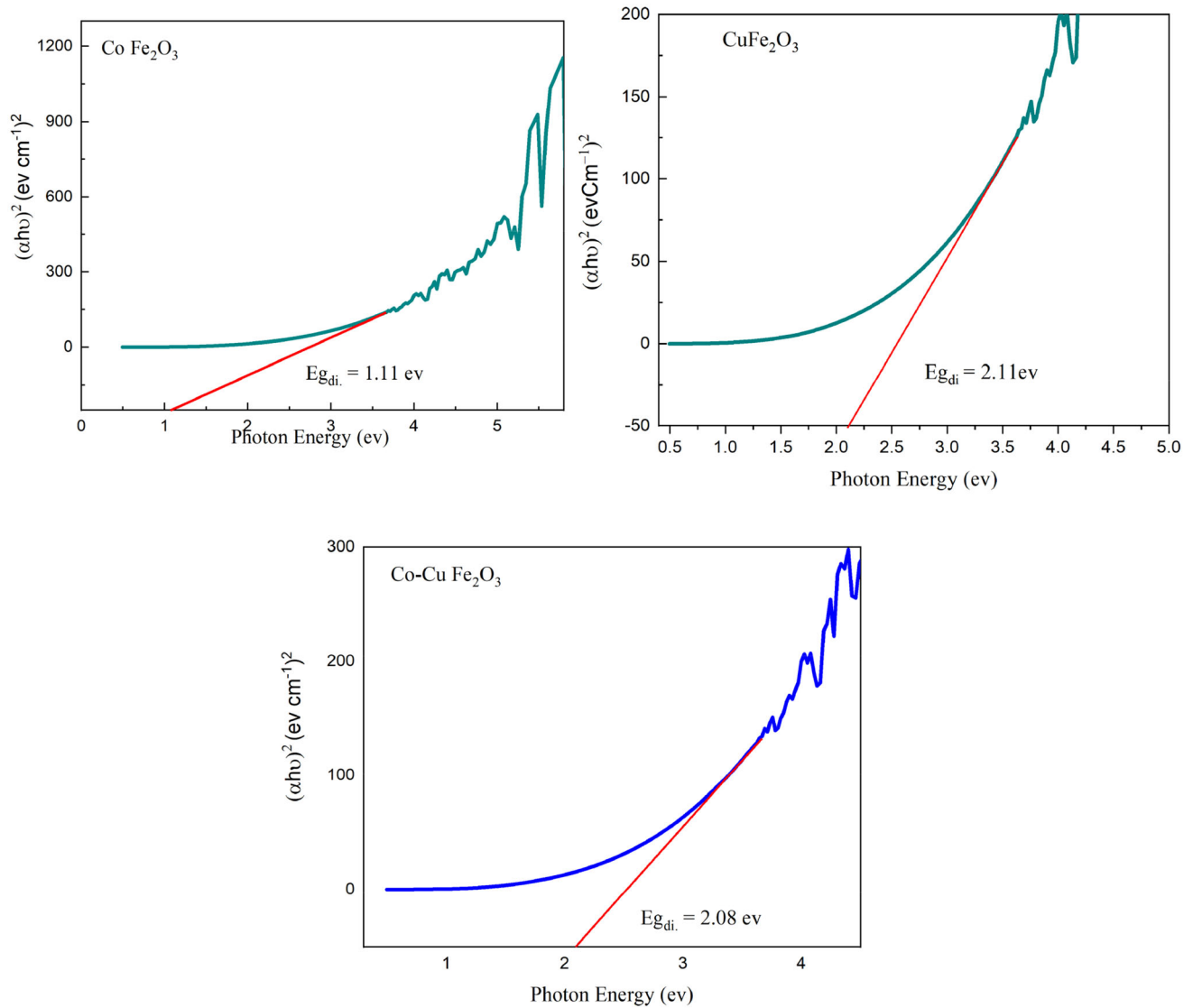


Fig. 8 Tauc plot for (a): CoFe₂O₄, (b): CuFe₂O₄, (c): Co-CuFe₂O₄

Table 4 Direct bandgap energy, Indirect bandgap energy and Urbach energy values of CoFe₂O₄, CuFe₂O₄ and Cu-CoFe₂O₄

Sample	Direct bandgap ($E_{g_{di}}$) (eV)	Indirect bandgap ($E_{g_{in}}$) (eV)	Urbach energy (E_U) (eV)
CoFe ₂ O ₄	1.11	0.078	0.22
CuFe ₂ O ₄	2.11	0.31	0.20
Cu-CoFe ₂ O ₄	2.08	0.32	0.26

nm. It can be noticed that all the investigated samples have high absorption coefficients in the visible range and they decrease with increasing wavelength. As shown in Fig. S3(a, b, and c), the Urbach energy tail is estimated by plotting $\ln(\alpha)$ vs. photon energy ($h\nu$). Fitting the linear portion of the curve with a straight line, the reciprocal of the slope yields the value of E_U . Smaller band tailing with $E_U = 0.2 \text{ eV}$ for CuFe₂O₄,

than that of $E_U = 0.22 \text{ eV}$ for CoFe₂O₄ was observed. And an increase of $E_U = 0.26$ for Cu-CoFe₂O₄ meaning incorporation of a greater number of localized defect states which widens the band tails.

3.2 Photocatalytic activity of the CoFe_2O_4 , CuFe_2O_4 , and $\text{Cu-CoFe}_2\text{O}_4$

Photoreduction of nitroaniline was performed with a CoFe_2O_4 catalyst, CuFe_2O_4 , and $\text{Cu-CoFe}_2\text{O}_4$ under visible light irradiation. The optical absorption experiments were performed after the adsorption equilibrium was obtained. Nitroaniline was used as a model substrate for the reaction, while Na_2SO_3 was used as a scavenger. The reaction progressed, analyzed by UV–Vis and Thin Layer Chromatography (TLC) analysis. The rates of nitroaniline reduction with CoFe_2O_4 , CuFe_2O_4 , and $\text{Cu-CoFe}_2\text{O}_4$ under visible light irradiation at 25 °C are shown in Fig. 9.

Interestingly, all the prepared materials exhibit a photoactive compound under visible light as shown in Fig. 9a. The photoreduction process can be expressed by pseudo-first-order and pseudo-second-order kinetics (Fig. 9b, c). $\text{Cu-CoFe}_2\text{O}_4$ showed higher rate constants compared to pure CuFe_2O_4 and CoFe_2O_4 . The catalytic reduction of nitroaniline was shown to follow the order: $\text{CoFe}_2\text{O}_4 < \text{CuFe}_2\text{O}_4 < \text{Cu-CoFe}_2\text{O}_4$. The constant (k_1) photoreduction rates of nitroaniline under visible light irradiation were 0.052, 0.061, and 0.079 min^{-1} for CoFe_2O_4 , CuFe_2O_4 , and $\text{Cu-CoFe}_2\text{O}_4$, respectively.

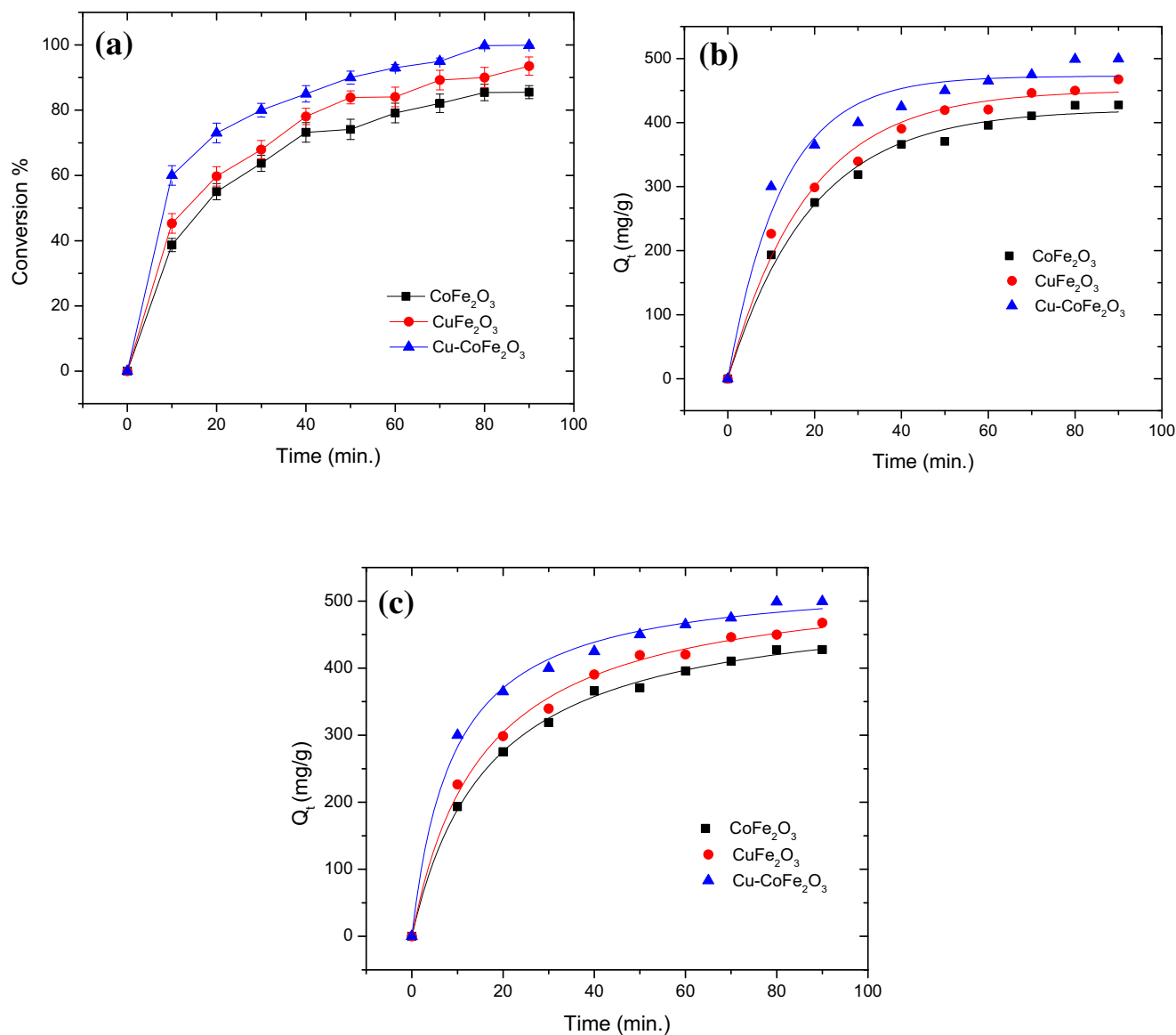


Fig. 9 Time dependent on the conversion of the reduction of nitroaniline

3.3 Recycling experiments

Although the CoFe_2O_4 , CuFe_2O_4 , and $\text{Cu-CoFe}_2\text{O}_4$ photocatalysts showed excellent nitroaniline reduction activity under visible irradiation, it was necessary to investigate the potential for reuse of the photocatalysts. Restoration of the stimuli was performed after the completion of the optical experiments. The photocatalysts were centrifuged at 5,000 rpm for 12 min with ethanol and the wet content was placed in an oven at 60°C overnight. The recovered photocatalysts were then used in the nitroaniline photoreduction experiments. Photocatalysts CoFe_2O_4 , CuFe_2O_4 , and $\text{Cu-CoFe}_2\text{O}_4$ showed excellent activity under experimental conditions and showed stability up to six cycles with the high throughput of aromatic amines (Fig. 10). The catalyst showed excellent stability with the metal content not being filtered out until six recycle experiments.

3.4 The possible mechanism for the photocatalytic reduction

However, we have suggested the potential reaction pathway for the photoreduction of nitroarenes into corresponding aromatic amines. The photosynthetic

reduction of nitroarenes continued through two potential pathways, comprising two reaction mediators, namely nitrous benzene and isobenzene. In another pathway, the nitrosobenzene as a reaction substrate under experimental conditions gives aniline as a product under similar conditions, which confirmed that the photocatalytic reduction of nitrobenzene occurred through the formation of a nitrobenzene medium (Fig. 11). The formation of aromatic amines occurred with a negative potential, which could be suitable in the conduction band of $\text{Cu-CoFe}_2\text{O}_3$ semiconductors. In the doping of copper on CoFe_2O_3 , the photocatalyst demonstrated a Z-diagram mechanism to improve the efficacy of nitrogen reduction under visible illumination. In a photocatalytic system, electrons in $\text{Cu-CoFe}_2\text{O}_3$ get excited under visible radiation and leave holes in VB, where Na_2SO_3 oxidizes to 6H^+ and 6e^- and satisfies the electron deficiency. These protons and generated electrons from this process were used to reduce the nitro group. Boosting the photocatalytic dehydrogenation of formic acid was done using Schiff-base-rich gC_xN_4 decorated PdAg nanowires [36].

Fig. 10 Recycling experiments of conversion for the reduction of nitroaniline

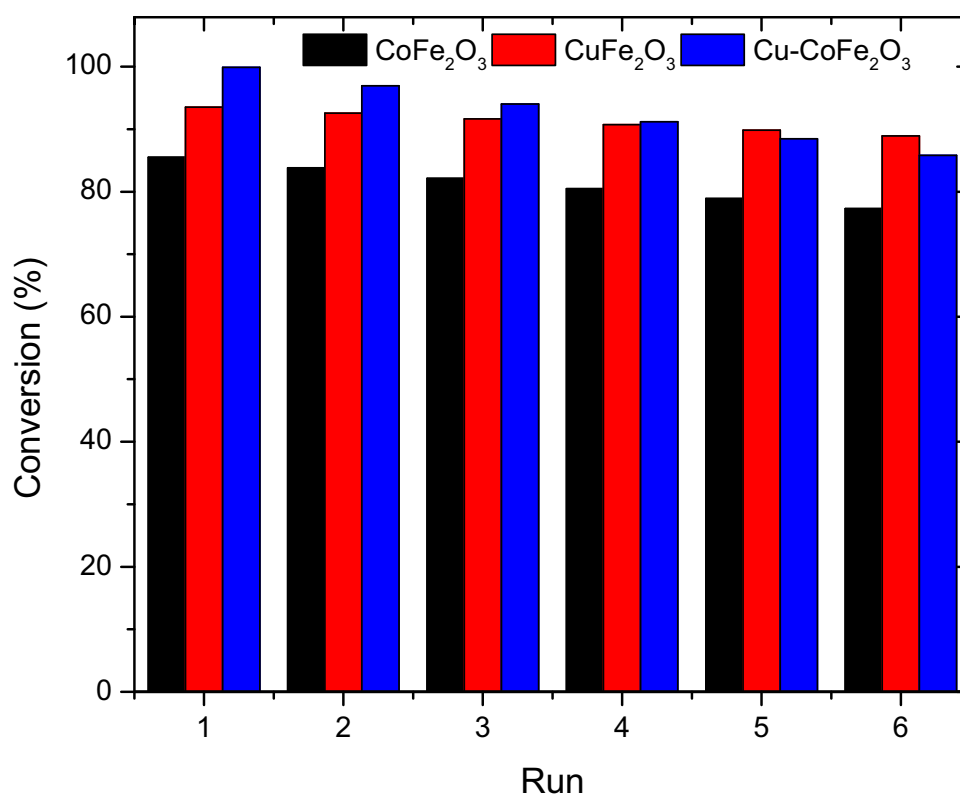


Fig. 11 Reaction pathway for nitroaniline reduction to amino-aniline

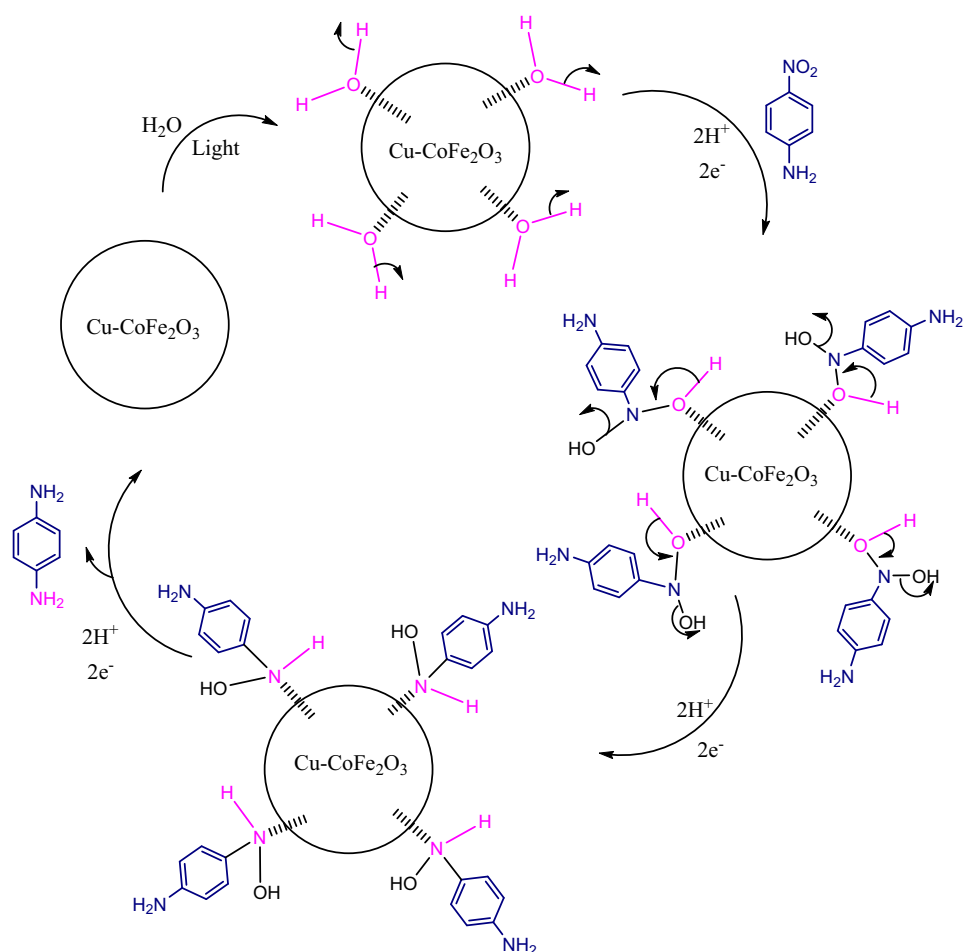


Table 5 Scope of the nitroarenes reduction under visible light using Cu-CoFe₂O₃ photocatalyst

Entry	Substrate	Product	Conversion	Yield	Selectivity
			(%)	(%)	(%)
1.			97	96	99
2.			98	95	98
3.			95	91	97
4.			96	93	97
5.			91	90	96
6.			98	95	99
7.			93	91	95

3.5 Photocatalytic nitroarenes reduction

Some different nitrobenzene compounds were used to test the efficacy of Cu-CoFe₂O₄ nanocatalyst. With the Cu-CoFe₂O₄ catalyst, a similar trend was observed for all light-substituting nitrobenzene compounds. The Cu-CoFe₂O₄ resulted in relatively higher conversion and throughput of the substrate and the product, respectively, under visible irradiation. The maximum conversion of nitroaromatic compounds was 99%, while the production of aminoaromatic compounds was 97% with the catalyst as shown in Table 5.

4 Conclusion

Briefly, the CoFe₂O₄, CuFe₂O₄, and Cu-CoFe₂O₄ photocatalysts were prepared by a simple hydrothermal precipitation method. The optical and structural properties were analyzed through various analytical methods. The photocatalytic performance of CoFe₂O₄, CuFe₂O₄, and Cu-CoFe₂O₄ showed a significant improvement with stable cycle performance. The magnetic behavior of the CoFe₂O₄, CuFe₂O₄, and Cu-CoFe₂O₄ helped to recover easily using an external magnetic rod. Thus, the photocatalysts CoFe₂O₄, CuFe₂O₄, and Cu-CoFe₂O₄ can be considered advanced suitable for the synthesis of organic chemicals used in the production of pharmaceutical intermediates.

Acknowledgements

The authors gratefully acknowledge the support provided by the national research centre, Cairo, Egypt in project ID (12020204).

Supplementary Information: The online version contains supplementary material available at <http://doi.org/10.1007/s10854-021-06387-3>.

References

1. N. Kerru, L. Gummidi, S. Maddila, K.K. Gangu, S.B. Jonnalagadda, A review on recent advances in nitrogen-containing molecules and their biological applications. *Molecules* **25**(8), 1909 (2020)
2. H.-Q. Zhao, Q. Liu, Y.-X. Wang, Z.-Y. Han, Z.-G. Chen, Y. Mu, Biochar enhanced biological nitrobenzene reduction with a mixed culture in anaerobic systems: short-term and long-term assessments. *Chem. Eng. J.* **351**, 912–921 (2018)
3. J.B. Lamture, *Aniline and Its Analogs* (Notion Press, Chennai, 2018)
4. R.M. Abdelhameed, M. Abu-Elghait, M. El-Shahat, Hybrid three MOFs composites (ZIF-67@ ZIF-8@ MIL-125-NH₂): enhancement the biological and visible-light photocatalytic activity. *J. Environ. Chem. Eng.* **1**, 17 (2020). <https://doi.org/10.1016/j.jece.2020.104107>
5. R.M. Abdelhameed, M. El-Shahat, Fabrication of ZIF-67@ MIL-125-NH₂ nanocomposite with enhanced visible light photoreduction activity. *J. Environ. Chem. Eng.* **7**(3), 103194 (2019)
6. H.E. Emam, H.B. Ahmed, E. Gomaa, M.H. Helal, R.M. Abdelhameed, Recyclable photocatalyst composites based on Ag₃VO₄ and Ag₂WO₄ @MOF@ cotton for effective discoloration of dye in visible light. *Cellulose* **27**, 7139–7155 (2020)
7. K. Imamura, S.-I. Iwasaki, T. Maeda, K. Hashimoto, B. Ohtani, H. Kominami, Photocatalytic reduction of nitrobenzenes to aminobenzenes in aqueous suspensions of titanium (IV) oxide in the presence of hole scavengers under deaerated and aerated conditions. *Phys. Chem. Chem. Phys.* **13**(11), 5114–5119 (2011)
8. H. Wang, J. Yan, W. Chang, Z. Zhang, Practical synthesis of aromatic amines by photocatalytic reduction of aromatic nitro compounds on nanoparticles N-doped TiO₂. *Catal. Commun.* **10**(6), 989–994 (2009)
9. S. Földner, T. Mitkina, T. Trottmann, A. Frimberger, M. Gruber, B. König, Urea derivatives enhance the photocatalytic activity of dye-modified titanium dioxide. *Photochem. Photobiol. Sci.* **10**(4), 623–625 (2011)
10. M. El-Shahat, A.E. Abdelhamid, R.M. Abdelhameed, Capture of iodide from wastewater by effective adsorptive membrane synthesized from MIL-125-NH₂ and cross-linked chitosan. *Carbohydr. Polym.* **231**, 115742 (2020)
11. H.E. Emam, M. El-Shahat, R.M. Abdelhameed, Observable removal of pharmaceutical residues by highly porous photoactive cellulose acetate@ MIL-MOF film. *J. Hazard. Mater.* **414**, 125509 (2021)
12. R. Abdelhameed, H. Abdel-Gawad, C. Silva, J. Rocha, B. Hegazi, A. Silva, Kinetic and equilibrium studies on the removal of 14 C-ethion residues from wastewater by copper-based metal–organic framework. *Int. J. Environ. Sci. Technol.* **15**(11), 2283–2294 (2018)
13. J. Wei, Y. Chen, H. Zhang, Z. Zhuang, Y. Yu, Hierarchically porous S-scheme CdS/UiO-66 photocatalyst for efficient 4-nitroaniline reduction. *Chin. J. Catal.* **42**(1), 78–86 (2021)

14. R.M. Abdelhameed, S.A. Al Kiey, A.R. Wassel, M. El-Shahat, Silver chromate doped Ti-based metal organic framework: synthesis, characterization, and electrochemical and selective photocatalytic reduction properties. *New J. Chem.* **45**, 9526–9537 (2021)
15. R.M. Abdelhameed, M. El-Shahat, H.E. Emam, Employable metal (Ag & Pd)@ MIL-125-NH₂@ cellulose acetate film for visible-light driven photocatalysis for reduction of nitro-aromatics. *Carbohydr. Polym.* **247**, 116695 (2020)
16. Q. Chang, H. Liang, B. Shi, X. Li, Y. Zhang, L. Zhang, H. Wu, Ethylenediamine-assisted hydrothermal synthesis of NiCo₂O₄ absorber with controlled morphology and excellent absorbing performance. *J. Colloid Interface Sci.* **588**, 336–345 (2021)
17. M. Qin, D. Lan, G. Wu, X. Qiao, H. Wu, Sodium citrate assisted hydrothermal synthesis of nickel cobaltate absorbers with tunable morphology and complex dielectric parameters toward efficient electromagnetic wave absorption. *Appl. Surf. Sci.* **504**, 144480 (2020)
18. Z. Ma, H. Tian, L. Cong, Q. Wu, M. Yue, S. Sun, A flame-reaction method for the large-scale synthesis of high-performance SmxCo_y nanomagnets. *Angew. Chem. Int. Ed.* **58**(41), 14509–14512 (2019)
19. Z. Ma, M. Yue, H. Liu, Z. Yin, K. Wei, H. Guan, H. Lin, M. Shen, S. An, Q. Wu, Stabilizing hard magnetic SmCo₅ nanoparticles by N-doped graphitic carbon layer. *J. Am. Chem. Soc.* **142**(18), 8440–8446 (2020)
20. Y. Slimani, E. Hannachi, in *Nanosensors for Smart Cities, Magnetic Nanosensors and their Potential Applications* (Elsevier, Amsterdam, 2020), pp. 143–155
21. M.A. Dar, J. Shah, W. Siddiqui, R. Kotnala, Study of structure and magnetic properties of Ni–Zn ferrite nano-particles synthesized via co-precipitation and reverse micro-emulsion technique. *Appl. Nanosci.* **4**(6), 675–682 (2014)
22. M.V. Gerbaldo, S.G. Marchetti, V.R. Elías, S.N. Mendieta, M.E. Crivello, Degradation of anti-inflammatory drug diclofenac using cobalt ferrite as photocatalyst. *Chem. Eng. Res. Des.* **166**, 237–247 (2021)
23. A. Khan, Z. Valicsek, O. Horváth, Synthesis, characterization and application of iron (II) doped copper ferrites (CuII (x) FeII (1-x) FeIII₂O₄) as novel heterogeneous photo-fenton catalysts. *Nanomaterials* **10**(5), 921 (2020)
24. E.Z. Hegazy, S.A. Kosa, I.H. Abd Elmaksod, J.T. Mojamami, Preparation, characterization and photocatalytic evaluation of aluminum doped metal ferrites. *Ceram. Int.* **45**(6), 7318–7327 (2019)
25. B.G. de Souza, G. Figueira, M.H. Carvalho, V. Alcaraz-Gonzalez, K.E. Saldaña-Flores, M. Godinho Jr., A.J. de Oliveira, R.H. Kiminami, L.A. Ruotolo, E.A. Urquieta-Gonzalez, A novel synthesis route to obtain magnetic nanocrystalline cobalt ferrite with photo-Fenton activity. *Mater. Chem. Phys.* **257**, 123741 (2021)
26. A. Tabasum, M. Alghuthaymi, U.Y. Qazi, I. Shahid, Q. Abbas, R. Javaid, N. Nadeem, M. Zahid, UV-accelerated photocatalytic degradation of pesticide over magnetite and cobalt ferrite decorated graphene oxide composite. *Plants* **10**(1), 6 (2021)
27. N. Gogoi, C.R. Gogoi, P.K. Gogoi, G. Borah, Versatility of magnetic Fe₃O₄ supported copper nanocomposite catalyst towards reduction of carbonyl and nitro compound. *Indian J. Chem.* **60**, 10–18 (2021)
28. M. Miranda, J. Sasaki, The limit of application of the Scherrer equation. *Acta Crystallogr. Sect. A* **74**(1), 54–65 (2018)
29. B.D. Cullity, J.W. Weymouth, Elements of X-ray diffraction. *Am. J. Phys.* **25**, 394 (1957)
30. M.M. El-Masry, R. Ramadan, M. Ahmed, The effect of adding cobalt ferrite nanoparticles on the mechanical properties of epoxy resin. *Results Mater.* **8**, 1160 (2020)
31. H.M.K. Tedjieukeng, P.K. Tsobnang, R.L. Fomekong, E.P. Etape, P.A. Joy, A. Delcorte, J.N. Lambi, Structural characterization and magnetic properties of undoped and copper-doped cobalt ferrite nanoparticles prepared by the octanoate coprecipitation route at very low dopant concentrations. *RSC Adv.* **8**(67), 38621–38630 (2018)
32. V.S. Kirankumar, S. Sumathi, Photocatalytic and antibacterial activity of bismuth and copper co-doped cobalt ferrite nanoparticles. *J. Mater. Sci.: Mater. Electron.* **29**(10), 8738–8746 (2018)
33. M.D. Donohue, G.L. Aranovich, A new classification of isotherms for Gibbs adsorption of gases on solids. *Fluid Phase Equilib.* **158–160**, 557–563 (1999)
34. Z. Li, R.-J. Xiao, P. Xu, C. Zhu, S. Sun, D. Zheng, H. Wang, M. Zhang, H. Tian, H.-X. Yang, Lattice dynamics and contraction of energy bandgap in photoexcited semiconducting boron nitride nanotubes. *ACS Nano* **13**(10), 11623–11631 (2019)
35. P. Jubu, F. Yam, V. Igba, K. Beh, Tauc-plot scale and extrapolation effect on bandgap estimation from UV–vis–NIR data—a case study of β-Ga₂O₃. *J. Solid State Chem.* **290**, 1276 (2020)
36. H. Liu, X.-X. Li, X.-Y. Liu, Z.-H. Ma, Z.-Y. Yin, W.-W. Yang, Y.-S. Yu, Schiff-base-rich gC x N 4 supported PdAg nanowires as an efficient Mott-Schottky catalyst boosting photocatalytic dehydrogenation of formic acid. *Rare Met.* **40**(4), 808–816 (2021)

Publisher's Note Springer Nature remains neutral with regard to jurisdictional claims in published maps and institutional affiliations.